RESEARCH ARTICLE

ADVANCED FUNCTIONAL MATERIALS
www.afm-journal.de

Anchoring Ultralow Platinum by Harnessing Atomic Defects Derived from Self-reconstruction for Alkaline Hydrogen Evolution Reaction

*Hancheng Ma, Wei Peng, Hoilun Wong, Xuyun Guo, Lin Xu, Mohsen Tamtaji, and Yao Ding**

The sluggish kinetics of alkaline hydrogen evolution reaction (HER) hinders practical exploitation of water splitting. Catalysts, known as platinum single atoms (Pt-SAs) anchored in Ni_4Mo/Ni alloys on nickel foam (Pt SAs-Ni_4Mo/Ni@NF) with ultralow Pt mass loading (m_{Pt} = 0.3 wt.%) derived from self-reconstruction, with boosted atomic utilization in alkaline HER are demonstrated. In situ characterizations confirm the leaching of Mo species during the self-reconstruction of $NiMoO_4$, which facilitates the anchoring of Pt-SAs through the generation of atomic defects. Further, density functional theory (DFT) calculations indicate that the atomic defects can effectively capture Pt^{2+} in salt solution, aiding in the distribution of Pt-SAs. Besides, theoretical results emphasize that Pt SAs-Ni_4Mo/Ni with unique Pt-Ni interaction can accelerate the desorption of hydroxides in alkaline electrolytes during HER, as well as lower energy barriers for reaction steps. Pt SAs-Ni_4Mo/Ni@NF shows remarkable catalytic activity toward alkaline HER with a low overpotential of 17 mV (j = 10 mA cm^{-2}), together with high atomic utilization of Pt (8.92 A mg_{Pt}^{-1} at 30 mV) and excellent durability. This work not only provides a scalable preparation for efficient and robust low-Pt catalysts but also establishes in-depth understanding of the synergistic interaction between Pt SAs and Ni-Mo alloys in alkaline HER, which is likely to accelerate the development of water-splitting technique.

1. Introduction

With its abundant supply and clean energy profile, hydrogen has emerged as a viable and environmentally friendly alternative to fossil fuels.[1] Its high energy density and efficient energy conversion make it a promising candidate for sustainably meeting energy needs. Hydrogen has been pursued as one of the most efficient and cleanest energy sources due to its environmentally friendly properties that can be produced by the electrochemical hydrogen evolution reaction (HER) in water splitting at cathodes.[2] Recent studies have explored the catalytic functionality of single-atom catalysts (SACs) for HER.[3] Moreover, due to the improved chemical and physical homogeneity of reaction sites, SACs often exhibit outstanding selectivity along with enhanced catalytic activity.[4] Among many types of SACs, Pt single atoms catalysts (Pt-SACs) have been considered to be the most promising ones for HER. However, there are currently many challenges in synthesis and stability for Pt-SACs, including the aggregation of Pt atoms and the loss of catalytic activity under harsh electrochemical conditions.[5] At the same time, the synthesis technology for SACs is complex and challenging to control, leading to a significant increase in costs.[6] Several researches for enhancing the stability and Pt utilization of Pt-SACs have been explored in recent years. For example, Pt-V_2CT_x was found by Park et al. showing excellent mass activity of Pt (7.88 A mg_{Pt}^{-1} @30 mV).[7]

H. Ma, W. Peng, Y. Ding
School of Materials Science and Engineering
Wuhan University of Technology
Wuhan 430070, P. R. China
E-mail: ydingaf@whut.edu.cn

H. Wong, M. Tamtaji
Department of Chemical and Biological Engineering and William Mong Institute of Nano Science and Technology
Hong Kong University of Science and Technology
Clear Water Bay, Kowloon, Hong Kong 999077, P. R. China

X. Guo
School of Chemistry
Centre for Research on Adaptive Nanostructures and Nanodevices and Advanced Materials Bio-Engineering Research Centre
Trinity College Dublin
Dublin D02PN40, Ireland

L. Xu
State Key Laboratory of Advanced Technology for Materials Synthesis and Processing
Wuhan University of Technology
Wuhan 430070, P. R. China

The ORCID identification number(s) for the author(s) of this article can be found under https://doi.org/10.1002/adfm.202409575

DOI: 10.1002/adfm.202409575

Fischer et al. developed N-doped carbon (MPNC) nanospheres in a pulsed Pt CVD process as superior HER Pt-SACs exhibiting 5.45 A mg_{Pt}^{-1} @20 mV.[8] However, the utilization of precious metals as catalysts is still insufficient to meet commercial demands, particularly in HER with alkaline electrolytes, which typically have sluggish kinetics compared to those in acid electrolytes.[9] Therefore, many strategies have been cultivated for the dispersion and stability of isolated Pt atoms on various supports, especially the atomic layer deposition (ALD), the metal-organic framework (MOF)-derived strategy, and vacancies/defects immobilized methodology, for the synthesis of SACs.[10] In order to anchor the single Pt atom, it is crucial to select a supporting substrate with strong binding energy.[11] The covalent interactions between Pt atoms and the corresponding substrates are studied and adjusted by using different substrates.[12] It is highly desirable to explore efficient Pt-SACs with suitable substrates to enhance reaction kinetics and minimize electricity consumption in alkaline HER.

$NiMoO_4$, a transition metal oxide, has attracted significant attention in the field of electrocatalysis due to its unique structural and electronic properties.[13] In recent years, extensive research efforts have been devoted to exploring the potential of $NiMoO_4$ as an efficient catalyst for oxygen evolution reaction (OER) under an alkaline environment. Several synthetic strategies are adopted to prepare $NiMoO_4$ on nickel foam (NF) and provide in situ techniques to characterize.[13,14] Interestingly, a drastic self-reconstruction of $NiMoO_4$ will occur during OER when exposed to oxidizing potentials that the catalyst transforms into the oxidic phase of NiOOH.[15] A structural change to electrochemically active metal oxyhydroxide and/or -oxide has also been found from $NiMoO_4$, facilitated by molybdate (Mo) leaching of the catalyst's counterpart which leads to the defects.[16] Currently, researches for $NiMoO_4$ mainly focuses on using restructuring phenomena to improve catalytic activity, with relatively rare analysis of the chemical valence states and structures of the restructuring products, which hinders further exploration of the reuse of these products.[17] Furthermore, the introduction of defects and vacancies in the material during restructuring creates additional active sites for hydrogen adsorption and promotes the dissociation of water molecules which results in enhanced catalytic kinetics and improved overall performance.[18] However, there is still no direct research on using self-reconstruction to introduce atomic-level doping of the electrochemical active metals in $NiMoO_4$ as high-performance catalysts.

Technologies face challenges of high Pt costs, stability issues, requiring for cost-efficiency, and sustainability. In this work, we provide a comprehensive synthesis to anchor ultra-low mass loading of Pt atoms (0.3 wt.%) in an alloyed host material (Ni_4Mo/Ni) by using the atomic defects derived from the reconstruction of $NiMoO_4$, which exhibits well performed catalytic properties in alkaline HER with a record high atomic utilization of Pt (η= 8.92 A mg_{Pt}^{-1} at 30 mV) and excellent durability with more than 100 h. During the self-reconstruction by OER, $NiMoO_4$ undergoes the leaching of Mo species and generates atomic defects (the "traps") which are crucial for the anchoring of Pt-SAs during a simple solution immersion with Pt-salts. Further annealing reduction can help to stabilize Pt atoms in the host materials and form Pt SAs-Ni_4Mo/Ni alloys which are confirmed with accelerated kinetics in the desorption of hydroxides in alkaline electrolyte during HER. In detail, these Pt SAs-Ni_4Mo/Ni@NF catalysts exhibit drastically enhanced alkaline HER activities with an ultralow overpotential of 17 mV at 10 mA cm^{-2} (vs 214 mV for $NiMoO_4$@NF and 68 mV for Ni_4Mo/Ni@NF). The improved performance of these Pt SAs-Ni_4Mo/Ni@NF catalysts can be attributed to the self-templated fabrication of $NiMoO_4$ nanorods and in situ creation of Pt SAs-Ni_4Mo/Ni@NF dual active components. The structural and electronic properties of Pt SAs-Ni_4Mo/Ni@NF, as well as the mechanisms underlying the catalytic activity, and the strategies employed to optimize the performance through electrochemical restructuring will be discussed in the following part. The insights gained from these studies can pave the way for the design and development of highly efficient and cost-effective electrocatalysts for renewable energy conversion and storage applications.

2. Results and Discussion

Ni-Mo alloys with ultralow mass loading of platinum single atoms on nickel foam (Pt SAs-Ni_4Mo/Ni@NF) are achieved by using the chemical reconstruction of $NiMoO_4$ nanorods to anchor Pt-SAs (details in Experimental Section, Supporting Information). **Figure** 1a is the schematic illustration of a typical process. $Ni(NO_3)_2$ and Na_2MoO_4 are used as precursors for $NiMoO_4$ which has been reported by our previous work.[19] First, $NiMoO_4$ nanorods are uniformly grown on nickel foam (NF) (Figure S1, Supporting Information) by hydrothermal method. After synthesis, chemical reconstruction through OER is conducted on $NiMoO_4$@NF to get the "traps" for Pt atoms. Here, during reconstruction, $NiMoO_4$ will suffer from the sustainable loss of Mo species (Mo species leaching), which brings out the structural integrity.[20] Detailed analysis of the reconstruction mechanism will be revealed by in situ characterizations in Figure 5. By precisely controlling the condition of chemical reconstruction, the reconstructed $NiMoO_4$ with different amounts of Mo defects (R-$NiMoO_4$ "traps") can be formed. Following with a simple Pt^{2+} impregnation (Pt-R-$NiMoO_4$) and annealing, Pt atoms can be stably anchored in the Ni-Mo alloys (Ni_4Mo/Ni) with ultralow loading mass (0.3 wt.%, resulting from ICP-OES in Table S1, Supporting Information). High-angle annular dark-field scanning transmission electron microscopy (HAADF-STEM) exhibited the crystalline morphology of Pt SAs-Ni_4Mo/Ni nanosheets (Figure 1b). Compared to the pristine $NiMoO_4$ (Figure S1, Supporting Information), Pt SAs-Ni_4Mo/Ni shows an obvious reconstructed structure with irregular surface steps. Typical selection area electron diffraction (SAED) patterns of Pt SAs-Ni_4Mo/Ni in Figure 1c show sets of concentric diffraction circles which belong to different crystal faces of Ni_4Mo and Ni (Figure S2, Supporting Information). This indicates that an intriguing composition-segregation effect occurs on the nanosheets during annealing. Besides, the atomic STEM image (Figure 1d) further confirms the composition-segregation in Pt SAs-Ni_4Mo/Ni. For example, the measured lattice spacing d = 0.209 nm matches well with the Ni_4Mo (121) lattice fringes, while d = 0.202 nm and d = 0.179 nm match with the Ni (111) and (200) lattice fringes, respectively. Further, the anchored Pt atoms and atomic defects caused by reconstruction can be clearly seen in Ni_4Mo lattices (Figure 1e). During the impregnation of Pt^{2+}, Mo vacancies will be stably occupied by Pt^{2+} and coupled with the Ni

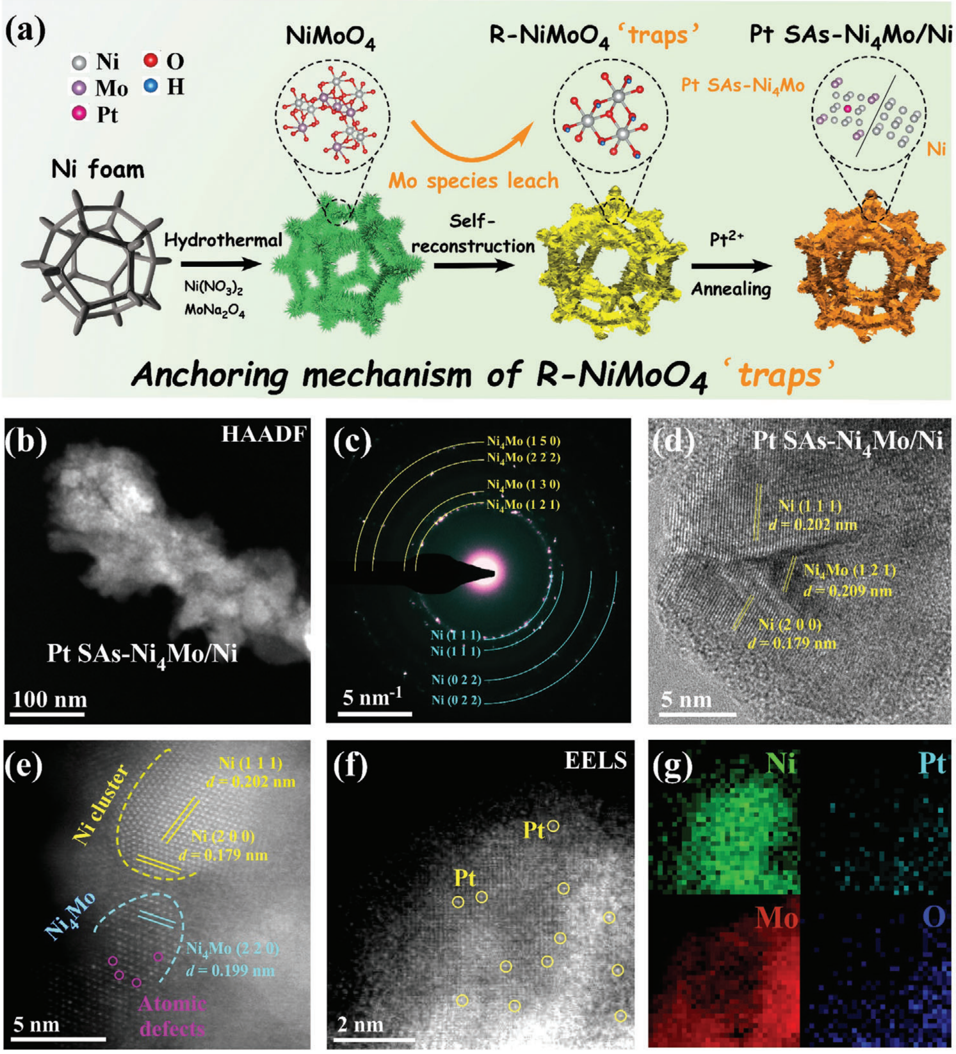

Figure 1. Synthesis of Pt SAs-Ni_4Mo/Ni and structural characterizations. a) Schematic illustration of the anchoring approach for ultralow Pt-SAs. b) HAADF-STEM and c) SAED indexed patterns of Pt SAs-Ni_4Mo/Ni. d) High-resolution STEM image and e) atomic construction of Pt SAs-Ni_4Mo/Ni where f) Pt single atoms located, and g) corresponding elemental distribution of (f) for Ni, Mo, Pt, and O.

oxides and hydroxides to form Pt SAs-Ni_4Mo/Ni after annealing. Figure 1f,g show the anchored Pt single atoms (Pt-SAs) in Ni_4Mo/Ni. The elemental distribution characterized by electron energy loss spectroscopy (EELS) shows that the anchored Pt atoms are mainly located in Ni_4Mo alloy instead of Ni. Here, signals of O elements are attributed to the small amount of MoO_{3-x} which are transformed from the unreconstructed $NiMoO_4$ after annealing.[21]

To further confirm the crystalline phase of Pt SAs-Ni_4Mo/Ni, X-ray diffraction (XRD) spectroscopy is employed to compare the crystalline phase of Pt SAs-Ni_4Mo/Ni with Ni_4Mo/Ni, R-$NiMoO_4$ and $NiMoO_4$ in **Figure** 2a, and the relevant PDF cards are shown in the Supporting Information. It can be clearly seen that after the electrochemical reconstruction, characteristic peaks of $NiMoO_4$ have been significantly weakened and disappeared, together with the appearance of peaks of $Ni(OH)_2$ in R-$NiMoO_4$. This is because of the intermediate products of reconstruction, e.g. NiOOH, are unstable and easily transformed into $Ni(OH)_2$. After annealing, R-$NiMoO_4$ will be reduced and form Ni_4Mo/Ni alloys, of which the peaks match well with the PDF cards of Ni_4Mo and Ni, corresponding to the above results in STEM. With the Pt^{2+} impregnation, Pt SAs-Ni_4Mo/Ni can be obtained with no distinguished new peaks compared with Ni_4Mo/Ni (details in the Experimental Methods). Furthermore, Fourier transform infrared (FT–IR) spectroscopy techniques are employed to illustrate the chemical changes of these products during the reconstruction and annealing process (Figure 2b). In the fingerprint regions of the FT–IR spectrum, the band at 959 cm^{-1} corresponds to the symmetrical stretching of $M=O$ bonds, while bands at 820 and 890 cm^{-1} correlate to the stretching vibrations of Mo—O—Mo bonds. Additionally, the sharp band at 745 cm^{-1} is attributed to the bending vibration of distorted MoO_4 units of $NiMoO_4$.[20] By comparing the FT–IR spectra of $NiMoO_4$ and R-$NiMoO_4$, it proves that the peak intensity of $M=O$ bonds and MoO_4 vibration units in R-$NiMoO_4$ significantly decreases, indicating the leaching of Mo species during OER reconstruction, which is further confirmed

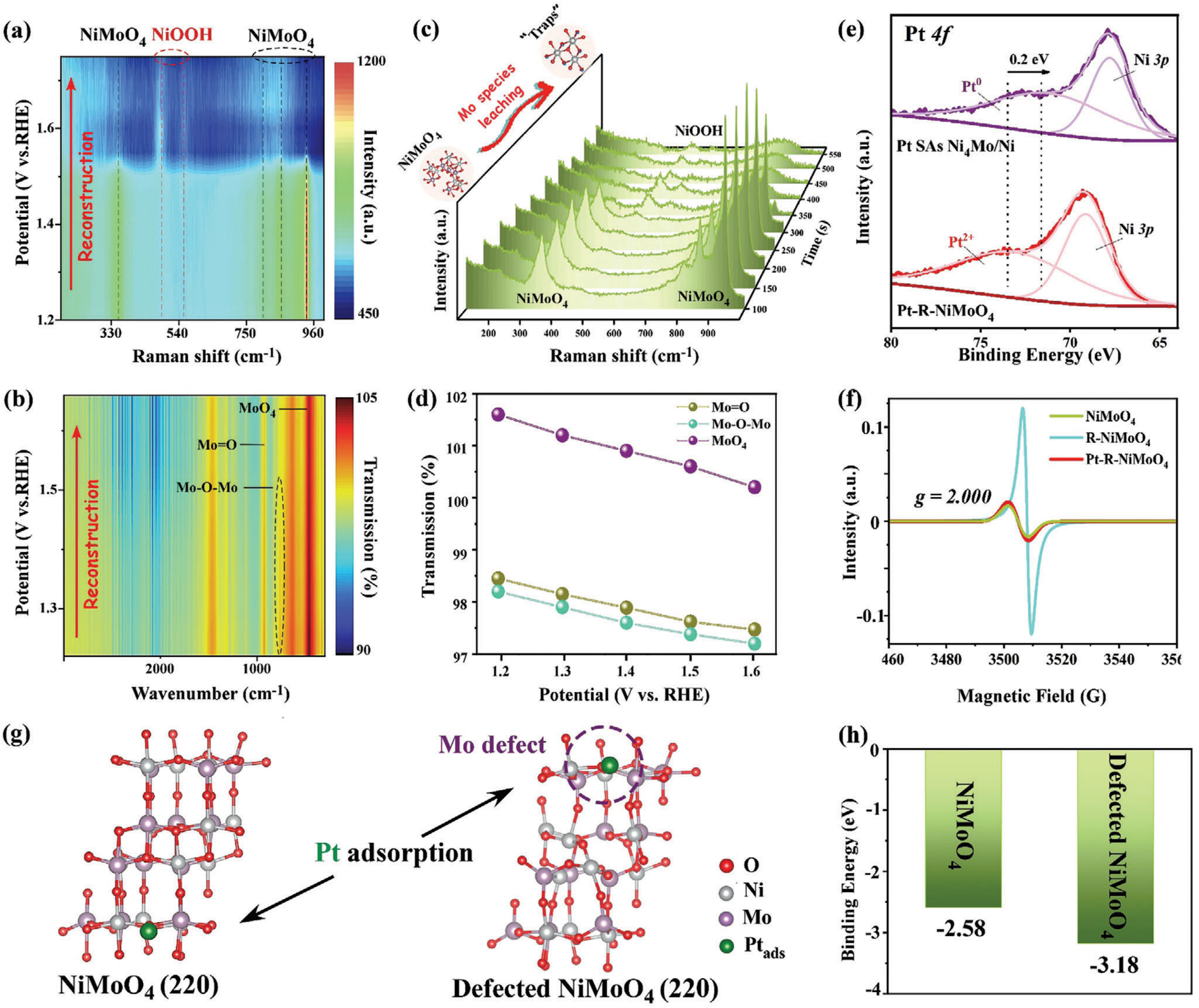

Figure 5. Formation and anchoring mechanism of the R-NiMoO$_4$ "traps" during reconstruction and Pt^{2+} impregnation. a) 2D contour diagram and b) 3D plot of in situ Raman characterization of NiMoO$_4$ over 550 s OER reconstruction. c,d) 2D contour diagram of in situ FT–IR spectroscopy for NiMoO$_4$ reconstruction (c), and the corresponding transmission changes of Mo ═ O, Mo—O—Mo and MoO$_4$ bonds e,f) EPR spectra of Pt-R-NiMoO$_4$, R-NiMoO$_4$ and NiMoO$_4$. g) Top view of the optimized structures of Pt atom absorbed on the surfaces of non-defected NiMoO$_4$ and defected NiMoO$_4$. h) Comparison of Pt binding energy in non-defected and defected NiMoO$_4$.

by Raman characterization (Figure S3, Supporting Information). After annealing and reduction, the disappearance of characteristic peaks of Mo—O bonds confirms that R-NiMoO$_4$ has been reduced. The chemical composition and the alloyed phase states of Pt SAs-Ni$_4$Mo/Ni are identified by X-ray photoelectron spectroscopy (XPS) as shown in Figure 2c–e. Besides, to characterize the stability of Pt-SAs in this catalyst for HER, XPS spectra of Pt *4f* in Pt SAs-Ni$_4$Mo/Ni and Pt SAs-Ni$_4$Mo/Ni post HER, which is tested by current parameters (CP) durability with $j = 10$ mA cm^{-2} for 100 h, are presented in Figure 2c. It can be clearly observed that Pt predominantly exists as Pt^0 states before and post HER,[22] demonstrating the stable metallic Pt single atoms on the surface of Ni$_4$Mo/Ni. The newly observed strong peak at the binding energy value of 67.7 eV for Pt SAs-Ni$_4$Mo/Ni is attributed to the Ni *3p* peak.[23] The Mo *3d* spectra (Figure 2d) exhibit dual peaks at 235.7 and 232.4 eV, corresponding to Mo *3d*$_{3/2}$ and Mo *3d*$_{5/2}$, respectively, with a spin-orbit coupling of 3.3 eV, which corresponds to Mo^{4+} in the NiMoO$_4$.[24] The Ni *2p* envelope can be deconvoluted into two spin-orbit components, Ni *2p*$_{3/2}$ and Ni *2p*$_{1/2}$ (Figure 2e). The binding energy peak at 855.6 eV and its satellite peak at 862 eV correspond to Ni *2p*$_{3/2}$, with the gap between the main binding energy peaks of Ni *2p*$_{3/2}$ and Ni *2p*$_{1/2}$ is 17.9 eV, indicating a Ni^{2+} oxidation state.[25] The Mo *3d* and Ni *2p* peaks of R-NiMoO$_4$ shift toward higher binding energy, indicating an increase in the valence state of the Ni and Mo elements following reconstruction. Additionally, Ni$_4$Mo/Ni and Pt SAs-Ni$_4$Mo/Ni shift toward the lower binding energy area. This is because the metal sites are reduced after annealing, leading to a decrease in the

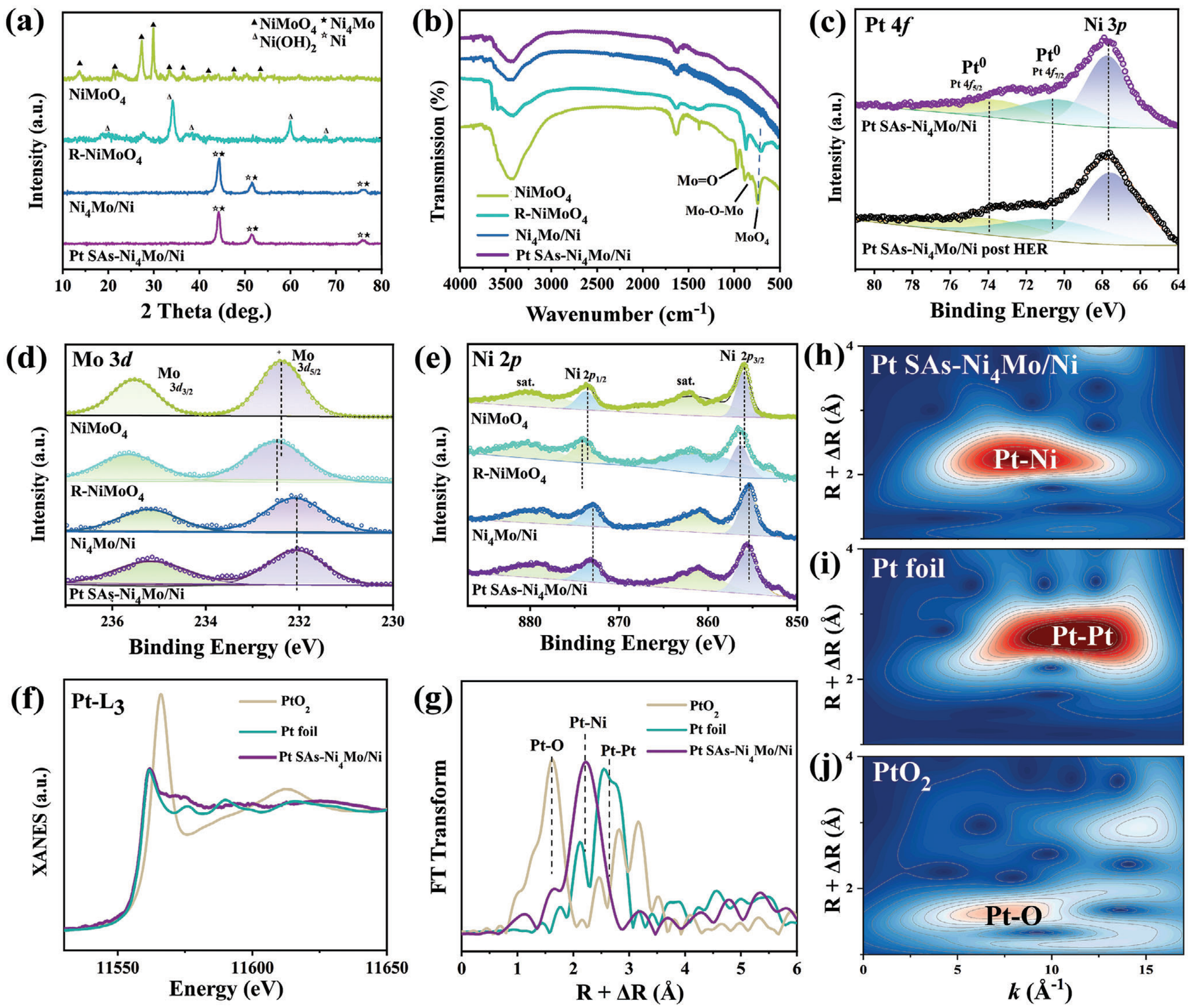

Figure 2. Characterization of phases and chemical coordination of Pt-Ni_4Mo/Ni. a) XRD patterns and b) FT–IR spectra of Pt SAs-Ni_4Mo/Ni, Ni_4Mo/Ni, R-$NiMoO_4$ and $NiMoO_4$. c) XPS spectra of Pt *4f* in Pt SAs-Ni_4Mo/Ni and Pt SAs-Ni_4Mo/Ni post HER (after 100 h stability test). d) XPS spectra of Mo *3d* and e) Ni *2p* in Pt SAs-Ni_4Mo/Ni, Ni_4Mo/Ni, R-$NiMoO_4$ and $NiMoO_4$. f) The comparison of XANES spectra of Pt L_3-edge, g) EXAFS shown in k^2 weighted R-space and h–j) wavelet-transform images of Pt-Ni_4Mo/Ni, Pt foil and PtO_2.

valence state and the formation of Ni_4Mo/Ni and Pt SAs-Ni_4Mo/Ni alloys.[26]

To further observe the Pt coordination in Pt SAs-Ni_4Mo/Ni, X-ray absorption spectroscopy (XAS) is applied to investigate the coordination and valence states of Pt compared with standard Pt foil and PtO_2. The oxidation state of Pt can be analyzed in a statistical manner from the X-ray absorption near-edge structure (XANES) region based on the Pt-L_3 edge position and white line intensity (Figure 2f). The results demonstrate that the Pt element in Pt SAs-Ni_4Mo/Ni is predominantly in a metallic state.[27] The Fourier transforms spectrum of the extended X-ray absorption fine structure (EXAFS) spectra of Pt are also investigated to study the atomic structure of Pt, as shown in Figure 2g. Generally, peaks located at 1.6 and 2.6 Å correspond to Pt-O and Pt-Pt, respectively.[28] The peak located at 2.27 Å corresponds to Pt-Ni coordination due to the anchored Pt SAs in Ni_4Mo, while Pt-Pt coordination is not observed showing that Pt exists in the form of single atoms rather than clusters (details in Supporting Information).[27] The wavelet transformation analysis of Pt SAs-Ni_4Mo/Ni, Pt foil, and PtO_2 are obtained in Figure 2h–j, which is further used to distinguish the Pt—Ni, Pt—Pt, and Pt—O bonds in different samples. Here, only one merged scattering path signal of the Pt—Ni bond located at $[\chi(k), \chi(R)]$ of [7.8, 2.27] is observed. At the same time, signals of Pt—Pt and Pt—O bonds located at [10.5, 2.61] and [7.5, 1.62] are obviously shown.[29] These results provide strong evidence for the existence of metallic single-atom platinum of Pt SAs-Ni_4Mo/Ni. By breaking the bonds between Mo and O atoms, a pathway is created for the subsequent incorporation of metal ions. Following the electrochemical reconstruction of $NiMoO_4$, we successfully introduced Pt doping to the

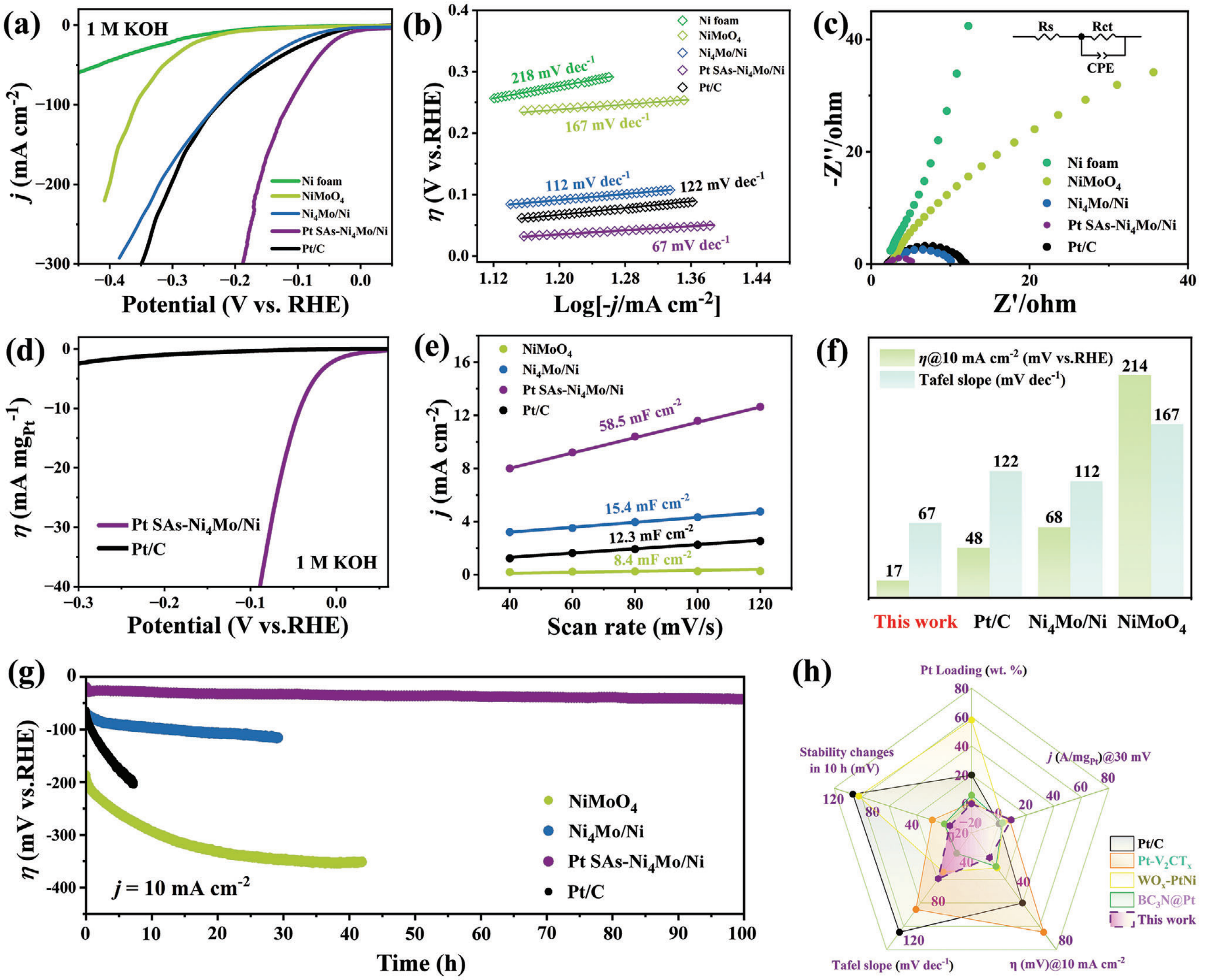

Figure 3. HER performance of Pt SAs-Ni$_4$Mo/Ni@NF. a) HER polarization curves and b) corresponding Tafel plots of Ni foam, NiMoO$_4$@NF, Ni$_4$Mo/Ni@NF, Pt SAs-Ni$_4$Mo/Ni@NF, and Pt/C@NF (20 wt.% Pt) in 1 м KOH at a scan rate of 5 mV s^{-1}. c) Nyquist plots of Ni foam, NiMoO$_4$@NF, Ni$_4$Mo/Ni@NF, Pt SAs-Ni$_4$Mo/Ni@NF, and Pt/C@NF at the same testing potential. d) The mass-normalized catalytic activities for Pt SAs-Ni$_4$Mo/Ni@NF, and Pt/C@NF. e) Extraction of the C$_{dl}$ for different catalysts. f) Overpotential and Tafel slope performance comparison histogram of different catalysts. g) Stability test of NiMoO$_4$@NF, Ni$_4$Mo/Ni@NF, Pt SAs-Ni$_4$Mo/Ni@NF, and Pt/C@NF. h) Radar chart for the performance comparation of Pt SAs-Ni$_4$Mo/Ni@NF with other reported Pt-based HER catalysts in 1 м KOH.

structural defects that formed after leaching through solution immersion. This allows for the better stability of Pt doping through chemical coordination proved by following electrochemical characterization in **Figure 3**.

The performance of Pt SAs-Ni$_4$Mo/Ni on nickel foam (NF) in HER is evaluated by using a three-electrode configuration (details in the Electrochemical Measurement part in Supporting Information). The experiments are conducted in 1 M KOH solution. All the sample names in Figure 3 are omitted from the "@NF" symbols for clarity. Figure 3a shows the linear sweep voltammogram (LSV) curves of Ni foam, NiMoO$_4$@NF, Ni$_4$Mo/Ni@NF, Pt SAs-Ni$_4$Mo/Ni@NF and Pt/C@NF (20 wt.% Pt). Typically, Pt SAs-Ni$_4$Mo/Ni@NF exhibits a low overpotential of 17 mV at the current density $j = 10$ mA cm^{-2}, which far exceeds that of Pt/C@NF (48 mV), Ni$_4$Mo/Ni@NF (68 mV) and NiMoO$_4$@NF (214 mV). To evaluate the atomic utilization of Pt-SAs in this catalyst, the mass-normalized catalytic performance is also evaluated in Figure 3d (details in Pt mass activities calculation of Supporting Information). It can be seen that Pt utilization of Pt SAs-Ni$_4$Mo/Ni@NF exhibits a recorded performance, i.e., 8.92 A mg$_{Pt}$$^{-1}$ at 30 mV, which is among the best of reported catalysts (Table S1, Supporting Information). Besides, Pt SAs-Ni$_4$Mo/Ni@NF catalysts present the promising Tafel slope of 67 mV dec^{-1}, which is much smaller than that of Ni$_4$Mo@NF (112 mV dec^{-1}), Pt/C@NF (122 mV dec^{-1}) and NiMoO$_4$@NF (167 mV dec^{-1}), respectively. Further, the improved HER performance of Pt SAs-Ni$_4$Mo/Ni@NF benefited from chemical reconstruction can be clearly seen in Figure 3f. The electrode kinetics for the samples are also characterized by electrochemical impedance spectroscopy (EIS) measurements (Figure 3c).

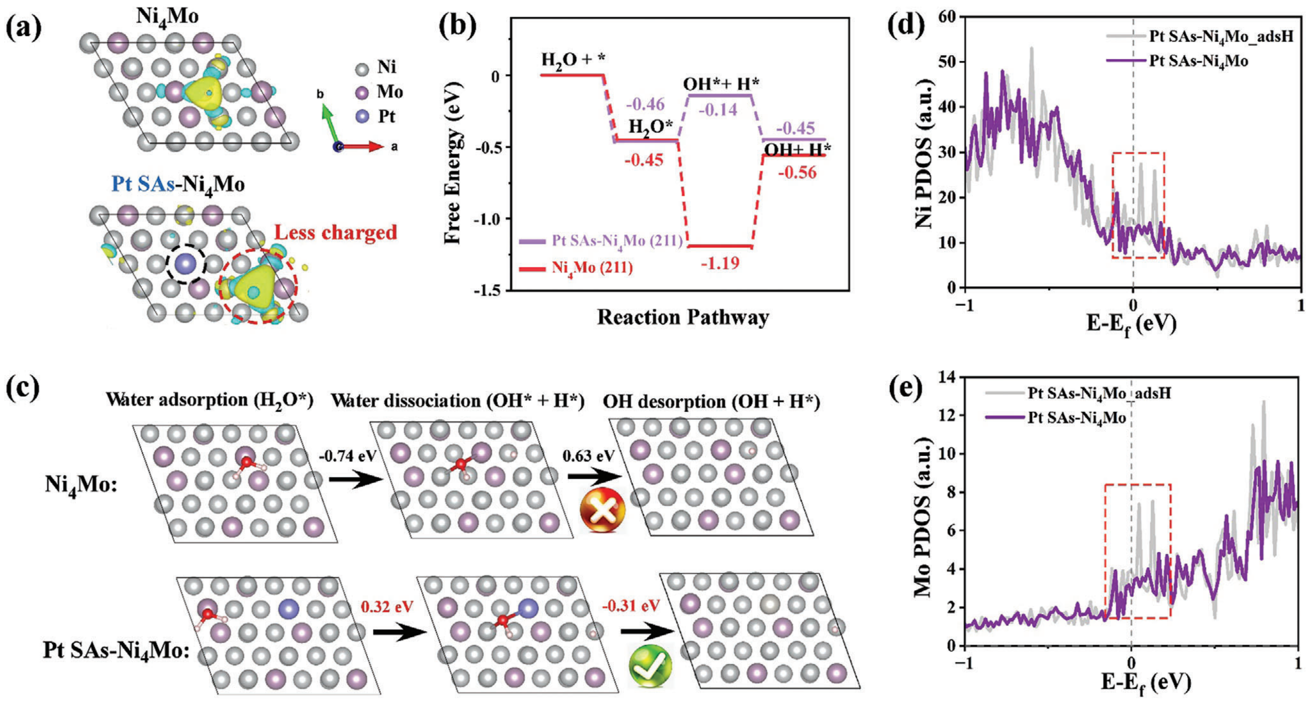

Figure 4. DFT calculations reveal the underlying mechanism of improved catalytic properties in alkaline HER. a) The charge differences between Ni_4Mo and Pt SAs-Ni_4Mo. b) The Gibbs free energy differences of different steps of alkaline HER in Ni_4Mo and Pt SAs-Ni_4Mo. c) Detailed reaction steps of HER in alkaline conditions for Ni_4Mo and Pt SAs-Ni_4Mo, including water adsorption (H_2O^*), water dissociation ($OH^* + H^*$) and hydroxide desorption ($OH + H^*$). For Ni_4Mo, the OH desorption is not spontaneous. d) Ni and e) Mo partial electron density of states (PDOS) of Pt SAs-Ni_4Mo and Pt SAs-Ni_4Mo_adsH.

The result shows that Pt SAs-Ni_4Mo/Ni@NF obtains a quite lower charge transfer resistance ($R_{ct} \approx 3.4\ \Omega$), indicating a faster electron transfer process compared with others.[30] Besides, as demonstrated in Figures 3e and S9 (Supporting Information), the charge transfer capacitance (C_{dl}) of Pt SAs-Ni_4Mo/Ni@NF (58.5 mF cm^{-2}) also surpasses that of Ni_4Mo/Ni@NF (15.4 mF cm^{-2}), Pt/C@NF (12.3 mF cm^{-2}), and $NiMoO_4$/NF (8.4 mF cm^{-2}) by a substantial margin. The superior performance of Pt SAs-Ni_4Mo/Ni@NF under alkaline conditions is related to its outstanding adsorption behavior, which is further confirmed in subsequent DFT calculations. Moreover, the long-term stability in alkaline HER for Pt/C@NF, $NiMoO_4$@NF, Ni_4Mo/Ni@NF, and Pt SAs-Ni_4Mo/Ni@NF are assessed through chronopotentiometry measurements (Figure 3g) at a constant current density of 10 mA cm^{-2}. Remarkably, after 100 h of continuous operation, Pt SAs-Ni_4Mo/Ni@NF exhibited superior stability compared to the others, indicating its exceptional durability. Furthermore, electrochemical in situ Raman and FT-IR measurements during HER are used to validate the chemical reconstruction of Pt SAs-Ni_4Mo/Ni, as shown in Figure S5 (Supporting Information). No significant intensity attenuation of the characteristic peaks in both Raman and FT–IR characterization indicates that there is no structural reconstruction of Pt SAs-Ni_4Mo/Ni during the HER process. Besides, other characterizations after the long-term stability test are shown in Figure S6 (Supporting Information). Remarkably, during the HER process in the alkaline electrolyte, a noticeable intensity enhancement of the Ni—O bonds is observed at a potential of 0.2 V versus RHE (Figure S5, Supporting Information). This is due to an optimal interaction with the OH_{ad} of Pt SAs-Ni_4Mo/Ni@NF, which facilitates the additional kinetics for HER.[28] Furthermore, Figure 3h provides a comprehensive comparison of HER performance of Pt SAs-Ni_4Mo/Ni@NF with a wide range of recently reported advanced catalysts (Table S2, Supporting Information). It clearly demonstrates that Pt SAs-Ni_4Mo/Ni@NF catalysts in this work exhibit outstanding alkaline HER performance in all respects, especially the atomic utilization of Pt-SAs. Besides, the benefits gained from chemical reconstruction are also proved by comparing with the electrochemical performance of Pt SAs-Ni_4Mo/Ni electrodes using the original $NiMoO_4$ precursor (Figure S7, Supporting Information).

To further explore the underlying mechanism in these improved alkalines HER catalytic performance, we replaced one Mo atom in the Ni_4Mo unit cell with a Pt atom (Pt SAs-Ni_4Mo) and conducted theoretical density functional theory (DFT) calculations by establishing a relevant model with (211) lattice fringes. **Figure 4a** illustrates the differential charge density distribution of Ni_4Mo and Pt SAs-Ni_4Mo (details in Figure S10, Supporting Information). The charge accumulation between H and Pt-Ni_4Mo is slightly less than that between H and Ni_4Mo. Here, the lower H binding energy (−0.687 eV) and smaller charge near H binding sites of Pt SAs-Ni_4Mo enable better catalytic performance.[28] Besides, Figure 4c shows three elementary steps of HER in alkaline conditions for Ni_4Mo and Pt SAs-Ni_4Mo: (1) water adsorption (H_2O^*); (2) water dissociation ($H^* + OH^*$); (3) OH desorption ($H^* + OH$). In addition, by calculating all steps in alkaline HER for Ni_4Mo and Pt SAs-Ni_4Mo, it can be found that Pt SAs-Ni_4Mo

shows much smaller Gibbs free energy (**Δ**G) for water dissociation step (−0.17 eV) than that of Ni_4Mo (−1.22 eV), which exhibits a better capability of water dissociation (Figure 4b; Table S3, Supporting Information).[31] The relatively smaller water dissociation energy facilitates the formation of adsorbed H^* on Pt SAs-Ni_4Mo in alkaline media, contributing to faster kinetics. Moreover, for Pt SAs-Ni_4Mo, all the steps are downhill energy barriers, while the OH desorption for Ni_4Mo is not spontaneous (**Δ**G = 0.9 eV). In order to further illustrate the structure-catalytic activities of Pt SAs-Ni_4Mo in HER through H adsorption, the partial electronic density of states (PDOS) of Pt SAs-Ni_4Mo and Pt SAs-Ni_4Mo after adsorption of H^* (Pt SAs-Ni_4Mo_adsH) are calculated in Figure 4d,e. By analysing the PDOS plots, the contribution of different elements in the HER process can be obtained.[32] Here, except Pt sites, Ni and Mo elements also can be identified as the active sites which can be clearly seen in the Ni and Mo PDOS plots. In detail, the red boxed areas in Figure 4d,e represent the contributions from d_{z2}, d_{yz}, d_{xz} orbitals of Ni PDOS and d_{yz}, d_{xz} orbitals of Mo PDOS near the Fermi level, which indicates that both Ni and Mo elements exhibit more active catalytic properties in Pt SAs-Ni_4Mo due to the enhance electronic conductivity. Therefore, by the formation of this unique Pt-Ni coordination in Ni_4Mo/Ni alloyed host, it is interesting that not only the activity of Pt sites is enhanced, but also the Ni and Mo sites are benefited.

To explore the formation mechanism of the "traps" for Pt-SAs intuitively during chemical reconstruction, in situ Raman and in situ FT-IR characterizations for the OER reconstruction of $NiMoO_4$ are conducted. **Figure** 5a,b represent the in situ Raman results of the OER reconstruction of $NiMoO_4$ in 1.0 м KOH. Here, in the non-faradaic region of controlled potential electrolysis, $NiMoO_4$ remains unchanged. At the potential of 1.5 V versus RHE, the reconstruction starts, which is observed by the instantaneous disappearance of the characteristic peaks at 355, 825, 875 and 948 cm^{-1} for $NiMoO_4$. This indicates the Mo species ($[MoO_4]^{2-}$) leaching and the formation of R-$NiMoO_4$ "traps". Only a small peak at ≈450 cm^{-1} appears, which could be attributed to $Ni(OH)_2$[33] possibly formed in a subsequent surface reaction involving the remaining nickel or nickel oxide from the catalysts and the electrolyte after molybdenum leaching. With the oxidation of Ni^{II} to Ni^{III}, the immediate emergence of Raman signals at 472 and 556 cm^{-1} (γ-NiOOH) is detected. These are in good agreement with the reported values of Ni—O vibration.[13,34] Furthermore, in situ FT–IR characterization in Figure 5c,d of $NiMoO_4$ is performed to support the changes of bonds during reconstruction. The weakened signal of Mo—O—Mo (889 cm^{-1}), Mo ═ O vibration (959 cm^{-1}), and MoO_4 species (747 cm^{-1}) can be clearly observed at the potential of 1.5 V versus RHE, which leads to the transformation of $NiMoO_4$ to γ-NiOOH.[20] After being soaked in a Pt organic solution, the "traps" from R-$NiMoO_4$ can capture Pt^{2+} to form Pt-R-$NiMoO_4$. Comparing the XPS spectra of Pt *4f* in Pt SAs Ni_4Mo/Ni and Pt-R-$NiMoO_4$, the captured Pt^{2+} valence state of Pt-R-$NiMoO_4$ can be clearly seen.

To further illustrate the anchoring mechanism of R-$NiMoO_4$ "traps", electron paramagnetic resonance (EPR) measurement is used to characterize the electronic states of $NiMoO_4$ after reconstruction. EPR profiles of Pt-R-$NiMoO_4$, R-$NiMoO_4$, and $NiMoO_4$ exhibit that the "traps" from R-$NiMoO_4$ possess a significantly stronger signal than that from Pt-R-$NiMoO_4$ and pristine $NiMoO_4$ at g = 2.000 (Figure 5f), corresponding to more unpaired electrons stemming from high-valence Ni in R-$NiMoO_4$ "trap" after reconstruction.[35] This indicates that the R-$NiMoO_4$ should have more Mo vacancies.[36] After immersing in the Pt^{2+} solution, some of these vacancies will be occupied, leading to a weakening in the Pt-R-$NiMoO_4$ EPR signal. Besides, DFT is involved for adsorption study of Pt on $NiMoO_4$ for illustrating the capture ability of these "traps". The top view of the optimized structures of the Pt atom absorbed on the surfaces of non-defected $NiMoO_4$ and defected $NiMoO_4$ with (220) lattice fringes is obtained in Figure 5g (other potential structures and relevant details are obtained in Figures S12 and S13, Supporting Information). From the calculations of several configurations, it can be seen that defected $NiMoO_4$ is more prone to adsorb Pt^{2+} in the solution. The comparison of Pt binding energy for non-defected and defected $NiMoO_4$ obtained by Figure 5h shows that Pt binding energy on defected $NiMoO_4$ (−3.18 eV) is stronger than that on non-defected one (−2.58 eV). This result successfully illustrates that defected $NiMoO_4$ has a stronger interaction with Pt.[37] Therefore, the "traps" generated through reconstruction within the $NiMoO_4$ structure not only can enhance the strong adsorption of Pt^{2+} on $NiMoO_4$, but also contribute to more stable bindings with Pt. This demonstrates the feasibility of electrochemical reconstruction for anchoring single atoms and provides valuable insights for the design of high-performance HER catalysts.

3. Conclusion

Herein, we have successfully synthesized Pt SAs-Ni_4Mo/Ni@NF by first using electrochemical reconstruction of $NiMoO_4$ to anchor Pt single atoms which is a unique alkaline HER-active catalyst, showing a remarkable catalytic activity toward a low overpotential of 17 mV (j = 10 mA cm^{-2}) and a Tafel slope of 67 mV dec^{-1}. At the same time, Pt SAs-Ni_4Mo/Ni@NF shows a record high atomic utilization of Pt (8.92 A mg_{Pt}^{-1}@30 mV). In situ characterizations prove that $NiMoO_4$ undergoes irreversible surface reconstruction. Further theoretical results prove that after the reconstruction of $NiMoO_4$, the "traps" generated from Mo defects can effectively adsorb and immobilize Pt^{2+} in the solution to assist in the formation of Pt-SAs. Besides, the alloyed host materials (Ni_4Mo/Ni) formed by annealing and reduction also exhibit contributed activities, as well as significantly increasing the utilization of Pt-SAs by the mutual interaction through electronic redistribution. In addition, compared with Ni_4Mo for all steps in alkaline HER, Pt SAs-Ni_4Mo exhibits the downhill energy barriers for all steps, especially with a much smaller ΔG = −0.76 eV for the water dissociation, which facilitates the formation of adsorbed H^* on Pt SAs-Ni_4Mo in alkaline media. In general, this work provides a novel approach for the fabrication of Pt-SACs and significantly boosts the potential exploitation of water splitting using low-cost and high-efficient catalysts toward hydrogen production. Besides, the strategy provided in this work has the potential to be applied in the field of oxygen reduction reaction (ORR) and zinc-air batteries, thereby expanding the utilization of noble metals to encompass multifunctional catalysis. Also, this efficient method for utilizing noble metals may also be extended to other transition metal (e.g., Co, Fe, etc.) based catalysts. Beyond this, the diverse properties of these catalysts can be applied in various fields, such as fuel cells, which enables the application and development of high-performance energy conversion devices.

Supporting Information

Supporting Information is available from the Wiley Online Library or from the author.

Acknowledgements

H.M., W.P., and H.W. contributed equally to this work. This work was financially supported by the National Key Research and Development Program of China (2023YFB3809301, 2020YFA0715000) and the National Natural Science Foundation of China (No. 61905183, 52127816).

Conflict of Interest

The authors declare no conflict of interest.

Data Availability Statement

The data that support the findings of this study are available from the corresponding author upon reasonable request.

Keywords

atomic utilization, hydrogen evolution reaction, $NiMoO_4$, self-reconstruction, ultralow platinum

Received: June 3, 2024
Revised: July 25, 2024
Published online:

---

[1] S. Mondal, S. Sarkar, D. Bagchi, T. Das, R. Das, A. K. Singh, P. K. Prasanna, C. P. Vinod, S. Chakraborty, S. C. Peter, *Adv. Mater.* **2022**, *34*, 2202294.
[2] X. Zou, Y. Zhang, *Chem. Soc. Rev.* **2015**, *44*, 5148.
[3] P. Kuang, Y. Wang, B. Zhu, F. Xia, C. W. Tung, J. Wu, H. M. Chen, J. Yu, *Adv. Mater.* **2021**, *33*, 2008599.
[4] Y. Shi, Z. R. Ma, Y. Y. Xiao, Y. C. Yin, W. M. Huang, Z. C. Huang, Y. Z. Zheng, F. Y. Mu, R. Huang, G. Y. Shi, Y. Y. Sun, X. H. Xia, W. Chen, *Nat. Commun.* **2021**, *12*, 3021.
[5] P. D. Tran, T. V. Tran, M. Orio, S. Torelli, Q. D. Truong, K. Nayuki, Y. Sasaki, S. Y. Chiam, R. Yi, I. Honma, J. Barber, V. Artero, *Nat. Mater.* **2016**, *15*, 640.
[6] S. Chen, S.-Z. Qiao, *ACS Nano* **2013**, *7*, 10190.
[7] S. Park, Y.-L. Lee, Y. Yoon, S. Y. Park, S. Yim, W. Song, S. Myung, K.-S. Lee, H. Chang, S. S. Lee, K.-S. An, *Appl. Catal., B* **2022**, *304*, 120989.
[8] S. Kuspert, I. E. Campbell, Z. Zeng, S. E. Balaghi, N. Ortlieb, R. Thomann, M. Knabbeler-Buss, C. S. Allen, S. E. Mohney, A. Fischer, *Small* **2024**, 2311260.
[9] K. Li, J. Zhang, R. Wu, Y. Yu, B. Zhang, *Adv. Sci.* **2016**, *3*, 1500426.
[10] a) L. Zhang, L. Han, H. Liu, X. Liu, J. Luo, *Angew. Chem. Int. Ed. Engl.* **2017**, *56*, 13694; b) N. Cheng, S. Stambula, D. Wang, M. N. Banis, J. Liu, A. Riese, B. Xiao, R. Li, T. K. Sham, L. M. Liu, G. A. Botton, X. Sun, *Nat. Commun.* **2016**, *7*, 13638.
[11] X. Wen, J. Guan, *Appl. Mater. Today* **2019**, *16*, 146.
[12] a) X. Wen, L. Bai, M. Li, J. Guan, *ACS Sustain. Chem. Eng.* **2019**, *7*, 9249; b) L. Bai, Z. Duan, X. Wen, R. Si, Q. Zhang, J. Guan, *ACS Catal.* **2019**, *9*, 9897.
[13] R. N. Durr, P. Maltoni, H. Tian, B. Jousselme, L. Hammarstrom, T. Edvinsson, *ACS Nano* **2021**, *15*, 13504.
[14] Z. Wang, H. Wang, S. Ji, X. Wang, P. Zhou, S. Huo, V. Linkov, R. Wang, *Chem* **2020**, *26*, 12067.
[15] a) B. R. Wygant, K. Kawashima, C. B. Mullins, *ACS Energy Lett.* **2018**, *3*, 2956; b) P. Zhou, X. Lv, S. Tao, J. Wu, H. Wang, X. Wei, T. Wang, B. Zhou, Y. Lu, T. Frauenheim, X. Fu, S. Wang, Y. Zou, *Adv. Mater.* **2022**, *34*, 2204089.
[16] L. Gao, X. Cui, C. D. Sewell, J. Li, Z. Lin, *Chem. Soc. Rev.* **2021**, *50*, 8428.
[17] Z. Wang, J. Chen, E. Song, N. Wang, J. Dong, X. Zhang, P. M. Ajayan, W. Yao, C. Wang, J. Liu, J. Shen, M. Ye, *Nat. Commun.* **2021**, *12*, 5960.
[18] Y. Chang, P. Zhai, J. Hou, J. Zhao, J. Gao, *Adv. Energy Mater.* **2021**, *12*, 2102359.
[19] X. Liu, J. Meng, J. Zhu, M. Huang, B. Wen, R. Guo, L. Mai, *Adv. Mater.* **2021**, *33*, 2007344.
[20] A. Rajput, M. K. Adak, B. Chakraborty, *Inorg. Chem.* **2022**, *61*, 11189.
[21] Y. Y. Chen, Y. Zhang, X. Zhang, T. Tang, H. Luo, S. Niu, Z. H. Dai, L. J. Wan, J. S. Hu, *Adv. Mater.* **2017**, *29*, 1703311.
[22] F. D. Speck, M. T. Y. Paul, F. Ruiz-Zepeda, M. Gatalo, H. Kim, H. C. Kwon, K. J. J. Mayrhofer, M. Choi, C. H. Choi, N. Hodnik, S. Cherevko, *J. Am. Chem. Soc.* **2020**, *142*, 15496.
[23] L. Wang, D. Mercier, S. Zanna, A. Seyeux, M. Laurent-Brocq, L. Perrière, I. Guillot, P. Marcus, *Corro. Sci.* **2020**, *167*, 108507.
[24] C. Chen, S. Wang, X. Luo, W. Gao, G. Huang, Y. Zeng, Z. Zhu, *J. Power Sources* **2019**, *409*, 112.
[25] C. Qing, C. Yang, M. Chen, W. Li, S. Wang, Y. Tang, *Chem. Eng. J.* **2018**, *354*, 182.
[26] a) D. Gazzoli, M. Occhiuzzi, A. Cimino, G. Minelli, M. Valigi, *Surf. Interface Anal.* **2004**, *18*, 315; b) E. S. Ilton, P. S. Bagus, *Surf. Interface Anal.* **2011**, *43*, 1549.
[27] J. Yang, R. Hubner, J. Zhang, H. Wan, Y. Zheng, H. Wang, H. Qi, L. He, Y. Li, A. A. Dubale, Y. Sun, Y. Liu, D. Peng, Y. Meng, Z. Zheng, J. Rossmeisl, W. Liu, *Angew. Chem. Int. Ed. Engl.* **2021**, *60*, 9590.
[28] Z. Wu, P. Yang, Q. Li, W. Xiao, Z. Li, G. Xu, F. Liu, B. Jia, T. Ma, S. Feng, L. Wang, *Angew. Chem. Int. Ed. Engl.* **2023**, *62*, e202300406.
[29] T. Xia, K. Zhao, Y. Zhu, X. Bai, H. Gao, Z. Wang, Y. Gong, M. Feng, S. Li, Q. Zheng, S. Wang, R. Wang, H. Guo, *Adv. Mater.* **2023**, *35*, 2206508.
[30] H. Song, Y. Li, L. Shang, Z. Tang, T. Zhang, S. Lu, *Nano Energy* **2020**, *72*, 104730.
[31] C. Zhang, X. Liang, R. Xu, C. Dai, B. Wu, G. Yu, B. Chen, X. Wang, N. Liu, *Adv. Funct. Mater.* **2021**, *31*, 2008298.
[32] J. Zhu, L. Cai, X. Yin, Z. Wang, L. Zhang, H. Ma, Y. Ke, Y. Du, S. Xi, A. T. S. Wee, Y. Chai, W. Zhang, *ACS Nano* **2020**, *14*, 5600.
[33] B. Kirubasankar, P. Palanisamy, S. Arunachalam, V. Murugadoss, S. Angaiah, *Chem. Eng. J.* **2019**, *355*, 881.
[34] a) S. Anantharaj, K. Karthick, S. Kundu, *Mater. Today Energy* **2017**, *6*, 1; b) Z. Qiu, C.-W. Tai, G. A. Niklasson, T. Edvinsson, *Energy Environ. Sci.* **2019**, *12*, 572.
[35] F. Biaso, B. Burlat, B. Guigliarelli, *Inorg. Chem.* **2012**, *51*, 3409.
[36] Z. Du, Y. Guo, H. Wang, J. Gu, Y. Zhang, Z. Cheng, B. Li, S. Li, S. Yang, *ACS Nano* **2021**, *15*, 19275.
[37] H. Zhang, Z. Wang, J. Ren, J. Liu, J. Li, *Energy Storage Mater.* **2021**, *35*, 88.